Measuring Chemical Shifts with Energy-Dispersive X-Ray Spectroscopy

Yueyun Chen,[1,2] Rebekah Jin,[1] Yarin Heffes,[1] Brian Zutter,[1,2] Tristan P. O'Neill,[1,2]
Jared J. Lodico,[1,2] B. C. Regan,[1,2] and Matthew Mecklenburg[2,*]
[1]*Department of Physics and Astronomy, University of California, Los Angeles, California 90095, USA*
[2]*California NanoSystems Institute (CNSI), University of California, Los Angeles, California 90095, USA*

(Received 25 September 2024; accepted 30 July 2025; published 8 October 2025)

Electron microscopy uses energy-dispersive x-ray spectroscopy (EDS) and electron energy loss spectroscopy (EELS) for elemental analysis. EDS and EELS energy resolutions are commonly between 30 and 100 eV or 0.01 and 1 eV, respectively. Large solid angle EDS detector technology has increased collection efficiency to enable precision spectroscopy via averaging of 0.02–0.1 eV. This improved precision gives access to chemical shifts; examples are shown in compounds of Al, Ti, and W. EDS can now detect chemical information in a complementary parameter space (accelerating voltage, thickness, atomic number) to that covered by EELS.

DOI: 10.1103/t1rs-7kr2

Transmission electron microscopy (TEM) can resolve atomic-level defects and interfaces inaccessible to other microscopy methods. These boundaries contain important chemical information [1]. Spectroscopies using x-ray sources for chemical detection, with energy resolution better than an eV, measuring absorption, emission, or photoelectrons, are spatially limited by these sources and optics to micrometer probe sizes or greater [2–4]. Spatial resolution using x-ray sources often does not surpass diffraction-limited optical microscope resolution [5]. In the far field, only TEM can access elemental and chemical information at the atomic level.

Scanning transmission electron microscopy (STEM) rasters a sub-Ångström sized probe to generate images in parallel with techniques like energy-dispersive x-ray spectroscopy (EDS) and electron energy loss spectroscopy (EELS) [6–9]. This pair of complementary spectroscopies measures the same inelastic events from different perspectives. EELS measures core electrons' binding energies after a primary electron inelastically scatters from a quantum bound state into a magnetic prism spectrometer. Combined high spatial and energy resolution delivers chemical shift mapping across atomically sharp interfaces [1,10]. EDS collects the emitted photon when a higher shell electron fills the hole vacated via inelastic scattering. EDS has comparatively poor energy resolution to EELS, but can detect a wider variety of elements.

Electrons pass through the sample before EELS captures them. The signal-to-background ratio (SBR) is kept high with minimal scatter [11,12]. Sharp edges (e.g., scattering from s and p orbitals) at large energy loss have small cross sections [13,14]. Scattering angle ranges can be categorized as $\theta_s = \Delta E/\gamma m_e v^2 \approx \Delta E/2KE$ (definitions in [15]), where $\Delta E/KE = 2\%$, 3%, and 4% for good, acceptable, and threshold ranges, respectively [16] [Fig. 1(a)]. For example, the Cu-K edge at 8,979 eV, was detected after a 10 nA 1 second exposure and fluence of $6 \times 10^9 - 3 \times 10^{11}\ e^-/\text{Å}^2$ [14] (depending if gun brightness or chromatic effects are considered). What is difficult to access with EELS can be complementarily captured by EDS, the Cu K shell efficiently acquired by x-rays being an example. Samples thick and thin can produce good x-ray spectroscopy, only limited by the overvoltage needed to excite the transition [Fig. 1(a)]. EDS chemical detection using electron sources, like that done using x-ray sources [4], can extend precision TEM spectroscopy into a new parameter space of thick samples, lower accelerating voltages, and transitions challenging to access by EELS.

Different x-ray spectrometer technologies have been used in TEM. Wavelength-dispersive x-ray spectroscopy (WDS) and microcalorimeters can both achieve sub-10 eV energy resolution when characterizing materials suitable for large beam currents and long exposure times [18–20]. The limited solid angle, serial collection, and moving parts make WDS less effective for TEMs. Microcalorimeters have cryogenic requirements and speed limitations making them (currently) adapted to specific acquisition applications where the higher expense can be justified [21,22]. In EDS, silicon drift detectors (SDD) [23] replaced silicon-lithium detectors SiLi [24] due to their high speed, larger solid angles, low cost, and lack of cryogen requirements [25]. SDD based EDS detectors are widely used on TEMs across the world and make up a large portion of the semiconductor industry's TEM workflow.

EDS instrumentation is less expensive than EELS by roughly an order of magnitude. No electron optics or

[*]Contact author: mmecklenburg@cnsi.ucla.edu

 © 2025 American Physical Society

associated alignments are needed [9]. EDS's high SBR, even with thick samples or low accelerating voltages, makes it suitable for both scanning electron microscopes (SEMs) and TEMs [26]. At 30 kV accelerating voltage EDS can already access the L line of all naturally occurring elements, whereas EELS efficiency [as in Fig. 1(a)] is good with lower atomic number elements (in s and p orbitals) and/or lower binding energies [27,28].

The SDD EDS [23] x-ray peak full width at half maximum (FWHM) is predominately determined by the electronic noise and shot noise fluctuation when converting photons into electron-hole pairs. An expression for this width measure is

$$FWHM_{EDS} = \sqrt{\left(2\sqrt{2\ln 2F\varepsilon_x\varepsilon_i}\right)^2 + \varepsilon_S^2 + \varepsilon_{LW}^2}, \quad (1)$$

where $\varepsilon_S \approx 30$ eV denotes the FWHM of the strobe peak [Fig. 1(b)], which arises from the electronic noise in the SDD [29], ε_{LW} denotes the natural line width of transition energy, typically a few eV. The others parametrize the photon to electron-hole pair conversion. The Fano factor, $F \approx 0.12$, quantifies the ionization correlations in silicon [30,31]. Parameters ε_x and ε_i (≈ 3.6 eV) are the x-ray energy and the silicon ionization energy, respectively [32,33].

For a W x-ray peak around 8 keV [W L_α for example, Fig. 1(b)], the EDS resolution is $FWHM_{EDS} \approx 140$ eV. This is 2 orders of magnitude larger than typical chemical shifts. Insufficient resolution does not translate to insufficient precision. Since SDD are nearly shot noise limited, averaging can improve precision until EDS becomes sensitive to sub-eV chemical shift. In Fig. 1(c) the measured chemical shift using curve fitting reveals a change just over half an eV [34]. Despite EDS being unable to resolve chemical shifts at the level of natural linewidth resolution, by collecting enough counts in the shot noise limited regime, better than 100 meV energy precision is achieved for well-isolated peaks [35]. With enhanced energy precision, EDS can be used for chemical shift measurement on heavy elements and even chemical shift mapping complementary to EELS.

To demonstrate EDS's capability of measuring chemical shifts, several compounds of tungsten (W), titanium (Ti), and aluminum (Al) are selected. The first two (acquired at 80 kV and 30 kV, respectively) cover regions that are EELS inefficient. The three W compounds [Fig. 2(a)] and three Ti compounds [Fig. 2(b)] are commercially available nanoparticles deposited on transmission electron microscope (TEM) grids with a thin carbon film (<10 nm) using standard drop-casting methods [36]. An aluminum film and an aluminum oxide film are deposited on a silicon nitride window using electron-beam evaporation and atomic layer deposition respectively [Fig. 2(c)]. The Al sample is microfabricated and the patterns of the two Al films are defined by optical lithography [37]. Multiple metal element compounds show how transition energy is affected by different chemical environments.

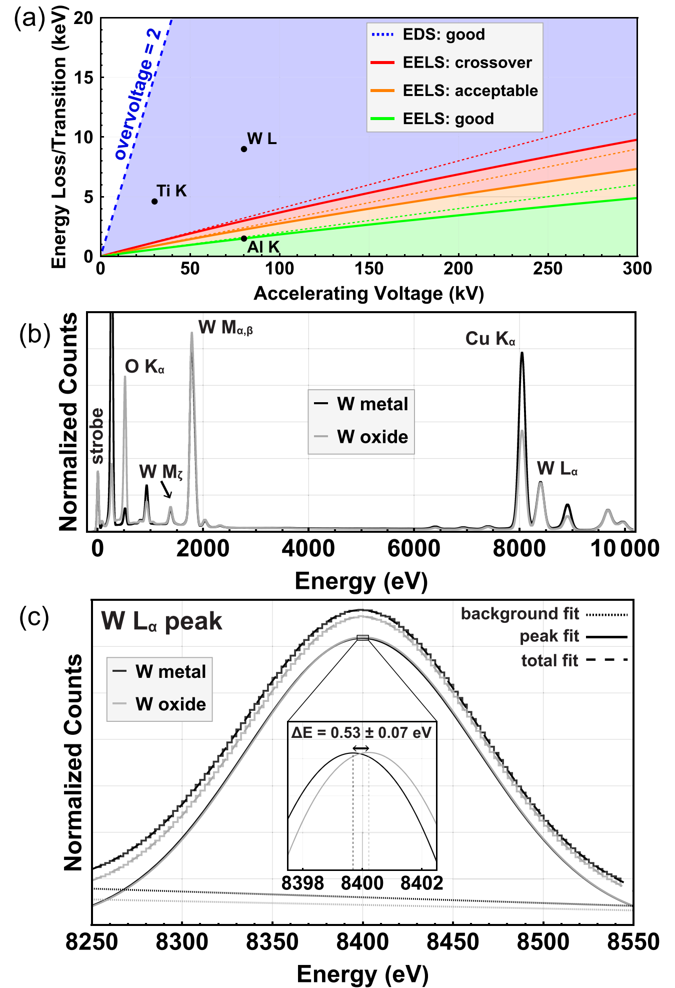

FIG. 1. (a) EDS and EELS detectable energy range plotted against the electron's accelerating voltage. EDS peak-to-background ratios and ionization cross sections are good with an overvoltage between 3 and 5 [17]; 2 is shown as a lower bound. Approximate EELS good (10 mrads), acceptable (15 mrads), and crossover (20 mrads) cases for efficient scattering angles are shown for relativistic (solid) and nonrelativistic (dashed) cases [16]. (b) EDS spectra from tungsten metal (black) and tungsten oxide (gray) acquired at 80 kV. (c) Curve fitting (Gaussian and linear background) to the W L_α peak. A chemical shift of 0.53 ± 0.07 eV is detected, and this shift is plotted in the inset.

For each W specimen, a spectrum is acquired in the highlighted region of interest (ROI) or across the entire field of view (FOV). For an EDS spectrum like the one shown in Fig. 1(b), the area under a certain peak is proportional to the corresponding elemental abundance, and any horizontal peak center shift is the transition energy's chemical shift. For Fig. 2(a) top and bottom specimens, W L_α and O K_α peaks are used to determine the stoichiometry and measure the averaged valence of W.

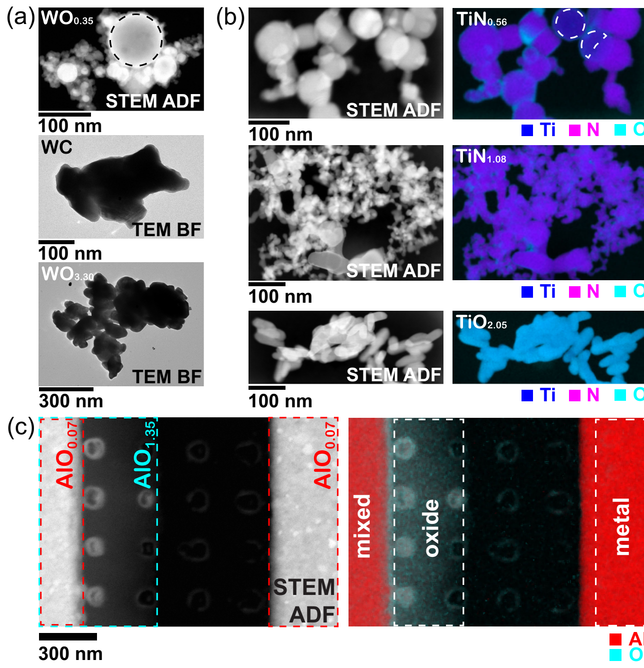

FIG. 2. Bright field TEM or annular dark field STEM survey images and EDS element concentration maps of the tungsten, titanium, and aluminum specimens. The labeled chemical compositions are measured within the ROI or across the entire FOV when no ROI is present. (a) Tungsten nanoparticles survey images. (b) Titanium nanoparticles survey images and EDS maps. (c) Aluminum films survey image and EDS map.

Following the Cliff-Lorimer method [26,38] and assuming oxygen having its most common valence −2, the composition is determined to be $WO_{0.35}$ and $WO_{3.30}$ respectively, which corresponds to a W averaged valence of +0.7 and +6.6 respectively. However, the carbon support membrane makes valence measurement infeasible for tungsten carbide [Fig. 2(a) middle], so the valence is taken to be +4 according to the manufacturer's 99.95% WC purity. For Ti and Al specimens, EDS spectrum images (where an EDS spectrum is acquired at each scan point in a raster pattern) are acquired, and elemental distributions are mapped. The valences of Al and Ti are determined the same way as the W specimens, and the chemical compositions are labeled in Figs. 2(b) and 2(c) [39].

The resolution of EDS is limited by the peak energy and electronic noise [Eq. (1)]. As the counts increase, curve fitting improves the precision. This enhanced precision, typically 3 orders of magnitude better than the FWHM resolution, provides chemical shift detection in EDS. In the shot noise limited regime, the uncertainty carried by individual x-ray measurement disturbs the curve fitting and limits the precision. As the number of counts N increases, the precision improves as a function of $\sqrt{N}$ [Fig. 3(a)]. This relationship is governed by Poisson statistics. As N increases, the precision vs counts curve flattens and approaches a limit. This asymptotic behavior arises from the SBR which is independent of the number of counts collected.

Solid state EDS detectors measure x-ray energy by collecting induced charges. A derived expression, the energy precision as a function of counts, is shown in Eq. (2). Poisson noise σ_p from the counting process and precision limit σ_0 contribute. The uncertainty σ_p comes from a single x-ray event. It is closely related to Eq. (1) empirically by $\sigma_p \approx 2FWHM/(2\sqrt{2\ln 2})$ [40]. Because of fluctuations in the ionization process, photons with the same energy do not always generate the same number of charges [30]. This leads to the uncertainty σ_p which is x-ray energy dependent, and its contribution to the total uncertainty can be reduced by collecting more x-ray events [41,42]. In the expression is described how precision changes as a function of counts,

$$\sigma_{\text{precision}} = \sqrt{\left(\frac{\sigma_p}{\sqrt{N}}\right)^2 + \sigma_0^2}, \tag{2}$$

σ_0 represents the highest precision achievable for a given peak, which is found to be negatively correlated with the SBR [43]. These two uncorrelated terms, σ_p and σ_0, add in quadrature and determine the total uncertainty of the measured x-ray energy. This empirical expression fits multiple datasets [Fig. 3(a)]. X-ray events are rare (roughly one x-ray photon is generated per 10 000 beam electrons [44]), but in solid state detectors collecting millions of counts is routine.

EELS chemical shifts in the binding energies of metal elements are always positive compared to pure metals [45], but EDS chemical shift in transition energies can be positive or negative [3,4,46–50]. In three W samples imaged at 80 kV, with 2.5 eV/channel bin size, chemical shifts are observed in five transitions lines ranging from 1 to 10 keV [Fig. 3(b)]. The three W L lines all have an energy higher than 7 keV, which is above the crossover regime for EELS [Fig. 1(a)]. W L_α and W $L_{\beta2}$ have positive chemical shifts less than +1 eV (about 1/3 of a spectrometer bin), and W L_λ has a negative chemical shift down to −2.6 eV (about one bin). Chemical shifts are also observed in W M_γ and W M2N4 lines, both negatively signed. Because of the high elastic to inelastic scattering cross section ratio and a short mean free path, W edges are very difficult to measure precisely with EELS. As an atom forms more bonds, the energies of core electrons are further minimized, which results in higher binding energies [51]. While EDS measures the energy difference between two electron orbits, whether the chemical shift is positive or negative depends on which electron's energy is minimized more when forming a new chemical bond. If the energy of the electron with a lower orbit is minimized more, the EDS chemical shift is positive, and vice versa. Thus, the observation of

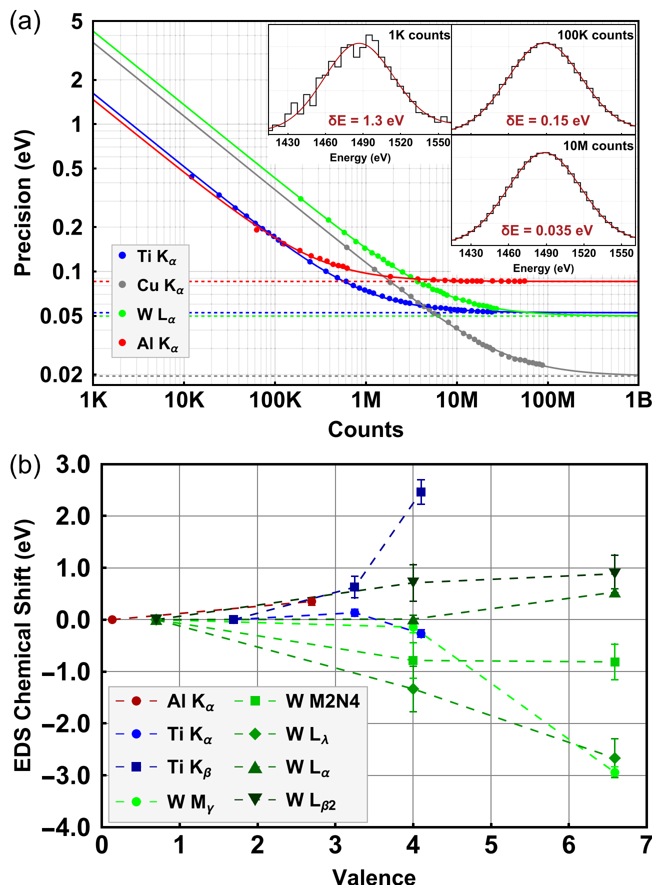

FIG. 3. (a) The precision (fit error in the mean) as a function of the number of x-ray counts detected for various elements and lines. The inset shows that as more x-ray events are collected, the Poisson noise is reduced, and the peak center can be determined more precisely. (b) EDS chemical shifts as a function of valence measured between covalently bonded compounds shown in Fig. 2. EDS measures the chemical shifts in transition energies that can be positive or negative.

both positive and negative chemical shift coincides with expectation.

In spectrum images acquired on Ti samples, spectra are summed inside the ROI or across the entire FOV. For Fig. 2(b) top, an ROI is applied to select nanoparticles with low nitrogen concentration to differentiate from Fig. 2(b) middle sample. The peak energies of Ti K_α and Ti K_β lines are measured by curve fitting. The Ti K_β line shifts up to +2.4 eV (about one bin), while the Ti K_α shifts less than 0.5 eV (Fig. 3). Acquired at 30 kV accelerating voltage, the 5 keV line is well over the crossover regime for EELS [Fig. 1(a)], but EDS can still provide precise information about the K shell. W and Ti measurements in the parameter space of large transition line and low accelerating voltage are inaccessible with EELS. By measuring Al K_α line around 1.5 keV (which is accessible with other TEM methods), the results are comparable with the literature. The spectrum image shows three distinct regions: mixed, oxide, and metal region [Fig. 2(c)]. The two ROIs in Fig. 2(c) bottom highlight the regions where only aluminum or aluminum oxide film exists. The spectra in the two ROIs are summed respectively, and the Al K_α chemical shift is determined to be +0.35 eV by curve fit, which is consistent with previous measurements [4,47] (the shift is about 1/14 the bin size). A tabulation of EDS chemical shifts is in the Supplemental Material [25].

Finally, to demonstrate our capability to map chemical shift, the aluminum EDS spectrum image is binned to have enough counts to fit the Al K_α line on pixel level. Three distinct regions are visible in the Al K_α energy map [Fig. 4(a)] together with the column-averaged plot [Fig. 4(b)]. The oxide region having a higher transition energy than the metal region indicates the Al K shell energy is minimized more than the L shell during the oxidation. A smooth transition is observed between the oxide and the mixed region and an oxide edge is detected at the edge of the metal region [Fig. 4(b)]. Even though the two peaks representing Al metal and oxide are not well separated in the histogram [Fig. 4(c)], a skewed normal distribution (for Al metal) and a normal distribution (for Al oxide) can be fitted to the distribution, and a shift of +0.36 eV is measured this way between the peak centers. This measurement on the histogram is in excellent agreement with the summed spectra measurement shown in Fig. 3(b). And it demonstrates that chemical shift mapping is possible with a 0.6 Sr solid angle single crystal detector [52].

For comparison, EELS and EDS spectrum images were collected in the same region under the same microscope settings. At 80 kV accelerating voltage, the Al K EELS is close to inefficiently measured, so only the Al $L_{2,3}$ edge is captured [53]. EELS is optically defined and the spectrum may drift after each scan pass. EDS can be mapped nearly indefinitely as spectra are not subjected to optical shifts. By measuring the Al $L_{2,3}$ edge location, a similar set of energy map and plots are generated [Figs. 4(d)–4(f)]. Three distinct regions are visible in the EELS Al $L_{2,3}$ energy map and column-averaged plot, and the two peaks for Al metal and oxide are well separated in the histogram. EELS differentiates the metal and the oxide better because the chemical shift in Al $L_{2,3}$ edge is an order magnitude greater than that in the Al K_α transition. It does not imply EELS has a better energy precision. In fact, for the Al metal region, the EDS energy map has 3 times better precision. EDS Al K_α line measures the Al K-$L_{2,3}$ transition energy, and EELS Al $L_{2,3}$ edge measures the Al $L_{2,3}$ binding energy. Combining them, the Al K 1s binding energy is determined to be 1559.95 ± 0.03 eV for Al metal and 1564.88 ± 0.04 eV for Al oxide, similar to results using EELS [2]. Being able to match EELS's energy precision and access a much higher energy range, EDS is a great complement for chemical shift analysis purposes. And in this specific case, EDS provides information EELS is missing about the Al K shell with comparable precision.

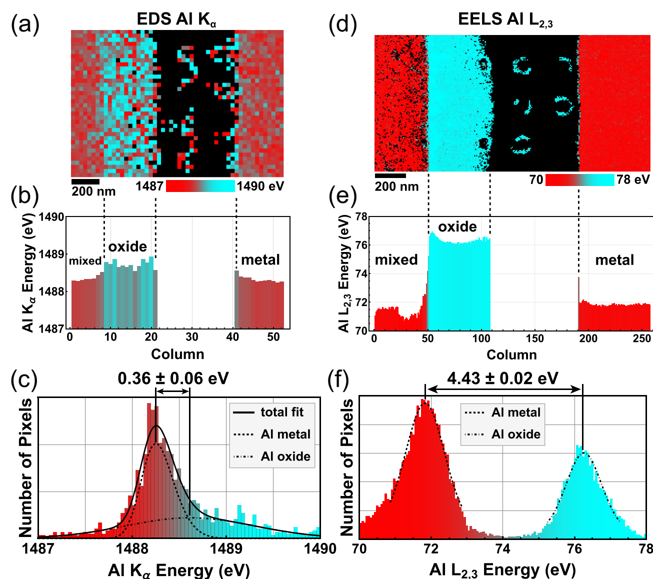

FIG. 4. (a),(d) EDS Al K_α energy map and EELS Al $L_{2,3}$ energy map. (b),(e) Column average plots of the energy maps above (columns with less than 50% convergent fits were omitted). Three distinct regions are visible in both EDS and EELS plots. (c), (f) Histograms of the energy maps (a), (d). Both histograms are fitted to two peaks representing the Al metal and oxide respectively. The EDS chemical shift is detectable despite being 12 times smaller than the EELS chemical shift.

Chemical analysis has long been the domain of EELS [11,12]. At lower accelerating voltages, the range of energies accessible with EELS decreases monotonically. EDS, in contrast, does not suffer from these constraints. EDS can be used over a wide range of accelerating voltages, sample thicknesses, and atomic numbers. The magnetic prism used to disperse electrons with different energies, although μ-metal armored, is susceptible to changes in the local magnetic field [11]. These changes can make the chemical shift difficult to detect, in particular when there is no zero-loss peak for reference. The zero-energy position in the EDS spectrum is nearly imperturbable, which allows adding spectra together from any time or position without any misalignment in energy [23]. Typically, EDS (EELS) is acquired over many frames (one frame) and a drift correction applied between frames (rows). An EDS system is more than an order of magnitude cheaper than conventional EELS systems. All these factors, versatility, stability, and cost, make it desirable to extend chemical analysis into the domain of EDS. EELS has enormous utility in the TEM, and now EDS can help in regions where EELS efficiency wanes while EDS efficiency complementary waxes.

EDS chemical shifts can be measured from a variety of compounds with sub-100 meV precision. These chemical shifts in transition energies can be either positive or negative, depending on the specific transition and chemical environment. Chemical shift mapping across an Al metal-oxide interface is demonstrated [Figs. 4(a)–4(c)] with a common SDD. The spatial resolution of EDS chemical shift mapping, fundamentally limited by the sample dependent x-ray generation volume, ranges from atomic level (sub-Ångström) to a few nanometers. Chemical shift maps in this work, limited by number of counts per unit area under the Al K_α peak, have a spatial resolution of about 30 nm. State-of-the-art SDDs can collect more than a million counts per second [8]. With such a detector, the minimal number of counts needed for chemical shift detection (10 k per peak) can be collected in 100 ms. EDS chemical shifts, in addition to being important for electron microscopy, can also be used in other systems using the same spectroscopy technique, such as x-ray florescent imaging.

Acknowledgments—We thank Lee Casalena and Huikai Cheng for their help in understanding and operating the TFS Spectra Ultra S/TEM with Ultra-X EDS. This work was supported by the Semiconductor Research Corporation (SRC), National Science Foundation (NSF) Award No. DMR-1611036, and NSF STC Award No. DMR-1548924 (STROBE). Data were collected at the Core Center of Excellence in Nano Imaging (University of Southern California), the Electron Imaging Center for Nanosystems (EICN) (RRID:SCR_022900) at the University of California, Los Angeles's California for NanoSystems Institute (CNSI), and the Thermo Fisher Scientific (TFS) Nanoport. Samples were fabricated in the Integrated Systems Nanofabrication Cleanroom (ISNC) at the California NanoSystems Institute (CNSI).

[1] D. A. Muller, Y. Tzou, R. Raj, and J. Silcox, Nature (London) **366**, 725 (1993).
[2] J. C. Sánchez-López, A. Caballero, and A. Fernández, J. Eur. Ceram. Soc. **18**, 1195 (1998).
[3] A. Braun, H. Wang, U. Bergmann, M. C. Tucker, W. Gu, S. P. Cramer, and E. J. Cairns, J. Power Sources **112**, 231 (2002).
[4] I. Lindgren, J. Electron Spectrosc. Relat. Phenom. **137–140**, 59 (2004).
[5] C. J. Blomfield, J. Electron Spectrosc. Relat. Phenom. **143**, 241 (2005).
[6] D. A. Muller, L. F. Kourkoutis, M. Murfitt, J. H. Song, H. Y. Hwang, J. Silcox, N. Dellby, and O. L. Krivanek, Science **319**, 1073 (2008).
[7] B. Goodge, A. Carlsson, M. Bischoff, A. Mohammadi-Gheidari, G. Fallag, G. Schwind, C. Maunders, D. Muller, and L. Kourkoutis, Microsc. Microanal. **26**, 1508 (2020).
[8] N. J. Zaluzec, Microsc. Microanal. **28**, 83 (2022).
[9] N. J. Zaluzec, Microsc. Microanal. **29**, 334 (2023).
[10] C. Colliex, L. Bocher, F. de la Peña, A. Gloter, K. March, and M. Walls, JOM **62**, 53 (2010).
[11] R. F. Egerton, Ultramicroscopy **107**, 575 (2007).

[12] R. F. Egerton, *Electron Energy-Loss Spectroscopy in the Electron Microscope* (Springer Science & Business Media, New York, 2011).

[13] I. MacLaren, R. B. Cummings, F. Gordon, E. Frutos-Myro, S. McFadzean, A. P. Brown, and A. J. Craven, in *Advances in Imaging and Electron Physics*, edited by P. W. Hawkes and M. Hÿtch (Elsevier, New York, 2019), Vol. 210, pp. 299–355.10.1016/bs.aiep.2019.02.001

[14] S. Lazar, P. Tiemeijer, C. S. Schnohr, M. Meledina, C. Patzig, T. Höche, P. Longo, and B. Freitag, Phys. Rev. Appl. **23**, 054095 (2025).

[15] $\gamma = 1 + \mathrm{KE}/m_e c^2$, KE is the electron's kinetic energy, m_e is the electron mass, v is the electron velocity, and c is the speed of light.

[16] I. MacLaren, K. J. Annand, C. Black, and A. J. Craven, Microscopy **67**, 78 (2017).

[17] H. Kohl and L. Reimer, in *Transmission Electron Microscopy: Physics of Image Formation*, Springer Series in Optical Sciences (Springer, New York, 2008), pp. 139–192.

[18] R. Castaing, Ph.D. thesis, University of Paris, 1951.

[19] D. A. Wollman, S. W. Nam, G. C. Hilton, K. D. Irwin, D. A. Rudman, N. F. Bergren, S. Deiker, J. M. Martinis, M. E. Huber, and D. E. Newbury, AIP Conf. Proc. **550**, 506 (2001).

[20] M. Terauchi, M. Koike, K. Fukushima, and A. Kimura, J. Electron Microsc. **59**, 251 (2010).

[21] D. A. Wollman, G. C. Hilton, K. D. Irwin, L. L. Dulcie, N. F. Bergren, D. E. Newbury, K.-S. Woo, B. Y. H. Liu, A. C. Diebold, and J. M. Martinis, AIP Conf. Proc. **449**, 799 (1998).

[22] T. Hayashi, R. Miyagawa, Y. Yagi, K. Tanaka, R. Ota, N. Y. Yamasaki, K. Mitsuda, K. Maehata, and T. Hara, J. Low Temp. Phys. **217**, 341 (2024).

[23] P. Lechner, S. Eckbauer, R. Hartmann, S. Krisch, D. Hauff, R. Richter, H. Soltau, L. Strüder, C. Fiorini, E. Gatti, A. Longoni, and M. Sampietro, Nucl. Instrum. Methods Phys. Res., Sect. A **377**, 346 (1996).

[24] R. Fitzgerald, K. Keil, and K. F. J. Heinrich, Science **159**, 528 (1968).

[25] See Supplemental Material at http://link.aps.org/supplemental/10.1103/t1rs-7kr2 section "Solid State Detector Evolution".

[26] J. I. Goldstein, D. B. Williams, and G. Cliff, in *Principles of Analytical Electron Microscopy*, edited by D. C. Joy, A. D. Romig, and J. I. Goldstein (Springer, Boston, MA, 1986), pp. 155–217.

[27] M. Isaacson and D. Johnson, Ultramicroscopy **1**, 33 (1975).

[28] R. D. Leapman and J. A. Hunt, Microsc., Microanal., Microstruct. **2**, 231 (1991).

[29] F. S. Goulding, Nucl. Instrum. Methods **142**, 213 (1977).

[30] W. Shockley, Solid-State Electron. **2**, 35 (1961).

[31] C. A. Klein, IEEE Trans. Nucl. Sci. **15**, 214 (1968).

[32] P. Lechner and L. Strüder, Nucl. Instrum. Methods Phys. Res., Sect. A **354**, 464 (1995).

[33] I. V. Kotov, H. Neal, and P. O'Connor, Nucl. Instrum. Methods Phys. Res., Sect. A **901**, 126 (2018).

[34] See SM section Error Analysis of Energy for example fitting residuals.

[35] The spectrometer bins and detector processing time are optimized to give the best precision and this process is discussed in the SM section Detector Optimization.

[36] See SM section on Sample Parameters for sample preparation and acquisition conditions.

[37] W. A. Hubbard, M. Mecklenburg, H. L. Chan, and B. C. Regan, Phys. Rev. Appl. **10**, 044066 (2018).

[38] G. Cliff and G. W. Lorimer, J. Microsc. **103**, 203 (1975).

[39] A comparison of valence values are tabulated in the SM section on Sample Parameters.

[40] See section Detector Optimization is the SM for further analysis.

[41] N. Kallithrakas-Kontos, Spectrochim. Acta B Atom. Spectros. **51**, 1655 (1996).

[42] Y. Xiao, S. Hayakawa, Y. Gohshi, and M. Oshima, Anal. Sci. **14**, 1139 (1998).

[43] See SI section Detector Optimization for SBR details.

[44] V. E. Cosslett, J. Microsc. **113**, 113 (1978).

[45] V. B. Sapre and C. Mande, J. Phys. C **5**, 793 (1972).

[46] T. C. Yao and J. J. Holst, Spectrochim. Acta B **23**, 19 (1967).

[47] P. G. Burkhalter, A. R. Knudson, D. J. Nagel, and K. L. Dunning, Phys. Rev. A **6**, 2093 (1972).

[48] J. Kawai, T. Konishi, A. Shimohara, and Y. Gohshi, Spectrochim. Acta B Atom. Spectros. **49**, 725 (1994).

[49] E. Boydaş, E. Orhan, M. G. Boydaş, and E. Cömert, Procedia—Social Behav. Sci. **195**, 1757 (2015).

[50] L. Miaja-Avila, G. C. O'Neil, Y. I. Joe, K. M. Morgan, J. W. Fowler, W. B. Doriese, B. Ganly, D. Lu, B. Ravel, D. S. Swetz, and J. N. Ullom, X-Ray Spectrom. **50**, 9 (2020).

[51] R. W. Carpenter, I. Chan, H. L. Tsai, C. Varker, and L. J. Demer, MRS Online Proc. Libr. **14**, 195 (1982).

[52] Another example of mapping is shown in SM section EDS Chemical Shift Map.

[53] An EELS chemical shift from the data in Fig. 4 is shown in Supplemental Material Fig. 10.